JOURNAL OF GEOPHYSICAL RESEARCH, VOL. 115, A12310, doi:10.1029/2010JA015866, 2010

Occurrence and properties of substorms associated with pseudobreakups

A. Kullen,[1] T. Karlsson,[1] J. A. Cumnock,[1,2] and T. Sundberg[1]

Received 26 June 2010; revised 30 July 2010; accepted 25 August 2010; published 8 December 2010.

[1] We investigate how substorms with and without growth-phase pseudobreakups are affected by solar wind and ionospheric conditions. The study is based on 874 events identified with Polar UVI. An AE index analysis shows that substorms with growth-phase pseudobreakups are typically weak and appear as isolated events after hours of low geomagnetic activity. During the hours before onset the average solar wind merging field E_m is weaker, and the length of time with enhanced values shorter than for regular substorms. Integrating E_m over the last southward IMF period before onset shows an upper limit above which these substorms do not occur. To estimate how much E_m reaches the ionosphere, polar cap potential drop and unified PC indices are examined. It is found that substorms with growth-phase pseudobreakups have on average lower PC index values than regular substorms. The temporal evolution of the PC indices is similar for both substorm groups; the summer index correlates better with E_m, the winter index with AE. Also the average polar cap potential drop curves for both types of substorms resemble one other; the dayside and nightside curves are mainly influenced by E_m and AE, respectively. Comparing growth-phase, isolated and recovery pseudobreakups shows that solar wind and ionospheric conditions around the first substorm after a pseudobreakup are similar, independent of whether the last pseudobreakup appeared hours (recovery and isolated pseudobreakups) or minutes before substorm onset (growth-phase pseudobreakups). Isolated and recovery pseudobreakups are less often associated with a northward IMF rotation than growth-phase pseudobreakups or substorms.

Citation: Kullen, A., T. Karlsson, J. A. Cumnock, and T. Sundberg (2010), Occurrence and properties of substorms associated with pseudobreakups, *J. Geophys. Res.*, *115*, A12310, doi:10.1029/2010JA015866.

1. Introduction

[2] The existence of pseudobreakups which appear just before substorm onset has been known for decades [*Elvey*, 1957]. However, pseudobreakups occur not only during the growth phase of a substorm, but also as isolated events during quiet times [*Fillingim et al.*, 2000] and at the end of substorm recovery [*Aikio et al.*, 1999].

[3] Recovery pseudobreakups appear close to the poleward oval boundary at the end of the recovery phase as isolated brightening and last even after the oval has retreated to its ground state [*Kullen and Karlsson*, 2004]. They may be regarded as a special type of poleward boundary intensification (PBIs). The latter occur frequently (mainly as multiple brightening) during substorm expansion and recovery at the poleward oval boundary [*Lyons et al.*, 1999], some of which develop into auroral streamers at the end of their lifetime [*Henderson et al.*, 1998]. It is in general difficult to discern between pseudobreakups (even isolated and growth-phase pseudobreakups), substorm breakup (onset) and PBIs, as all three types of auroral intensifications show the same auroral and magnetospheric signatures. That pseudobreakups and PBIs cannot be distinguished from substorm onset intensifications has been reported by *Ohtani et al.* [1993] and *Rostoker* [1998], respectively. Also, there seems to be a smooth transition between isolated pseudobreakups and very small substorms [*Kullen and Karlsson*, 2004, and references therein]. *Sergeev et al.* [1996] and *Rostoker* [1998] proposed, that all types of local auroral intensifications represent the same basic type energy dissipation into the ionosphere. They suggested that only those breakups with a source region close to the Earth develop into a global substorm, while intensifications with further tailward source regions do not expand globally. Several other researchers have been suggesting similar ideas, describing pseudobreakups as the smallest type of a substorm [e.g., *Nakamura et al.*, 1994; *Aikio et al.*, 1999].

[4] Most scientists assume the solar wind energy to be ultimately responsible for which type of auroral intensification that appears. *Kullen and Karlsson* [2004] showed that this holds true on a statistical basis since most pseudobreakups appear when the magnetic solar wind energy flux has very low values. A larger magnetic energy flux is connected to the

[1]Space and Plasma Physics, School of Electrical Engineering, Royal Institute of Technology, Stockholm, Sweden.
[2]Center for Space Sciences, University of Texas at Dallas, Richardson, Texas, USA.

0148-0227/10/2010JA015866

occurrence of stronger substorms. The question whether changes in the solar wind energy transfer into the magnetosphere may prevent an auroral intensification from expanding globally, i.e., becoming a pseudobreakup, remains open. Different answers have been given depending on the studied cases. *Rostoker* [1998] suggested that pseudobreakups do not expand globally due to a continued increasing energy input, *Partamies et al.* [2003] proposed that a sudden energy decrease may cause pseudobreakups, while *Nakamura et al.* [1994] assumed that the reason for the appearance of pseudobreakups is that not enough energy is stored in the magnetosphere.

[5] In this work we reinvestigate the question about what may prevent an auroral breakup to develop into a full-scale substorm. For this purpose, the large substorm and pseudobreakup event list from *Kullen and Karlsson* [2004] is used and compared to solar wind and ionospheric parameters. To find out about possible differences between substorms that are preceded by growth-phase pseudobreakups (pb substorms) and substorms where no growth-phase pseudobreakup appears before onset (regular substorms), in the first part of the study, solar wind conditions and ionospheric response are investigated for both substorm groups separately. In the second part, solar wind and ionospheric characteristics for different pseudobreakup types are examined and compared to each other.

2. Data Sources

2.1. Polar UV Images

[6] The UV experiment is one of four instruments of the Polar spacecraft. It is a two dimensional spatial imager which produces global images of the Earth's auroral regions in the far ultraviolet wavelength range [*Torr et al.*, 1995]. In winter 1998/1999, the UV instrument provided global auroral images of the Northern Hemisphere during approximately 10 h of each 18 h orbit. During an additional 4 h, at least some part of the oval was visible. The resolution of the images is 0.5 degrees in latitude at apogee; thus a single pixel projected to 100 km altitude from apogee is approximately 50 × 50 km. Away from apogee the imager can detect even smaller spatial scales. The UV camera images the aurora every 37 s in the ultraviolet region of the spectrum using four narrow band filters. The integration times are 18 and 36 s, respectively. For the identification of substorms and pseudobreakups, images taken with the LBH long filter has been chosen, where wavelengths between 164 nm and 178 nm are passed. Since the emissions in the wavelengths passed by the filter are not significantly absorbed by the atmosphere, the intensity of the emission is nearly directly proportional to the electron energy flux into the ionosphere. In order to detect even weak intensifications, only those images with a long integration time of 36 s have been selected, and the color scale has been fixed for all images at the lower end of the luminosity scale, spanning from 2 to 20 photons/cm2.

2.2. OMNI Solar Wind Data

[7] For the analysis of solar wind conditions around pseudobreakups and substorm breakups, 1 min resolution solar wind data from the OMNI data set are used (available at http://omniweb.gsfc.nasa.gov). That data set consists of measurements from the nearest solar wind monitor at each given point of time, the propagation time to the Earth bow shock is already included [*King and Papitashvili*, 2005].

2.3. AE Index

[8] To study the temporal evolution of the global auroral activity, 1 min resolution AE index data is downloaded from the WDC-C2 Kyoto AE index service (available at http:/swdcdb.kugi.kyoto-u.ac.jp/aedir/ae1/quick.html). The AE index (defined as the difference between the maximum geomagnetic variation at any of 12 stations spread over the auroral zone, and the corresponding minimum variation) gives a good estimation of the global evolution of auroral substorms.

2.4. Unified PC Indices

[9] The unified northern (PCN) and southern (PCS) polar cap indices monitor continuously geomagnetic activity over the northern (at Qaanaaq/Thule in Greenland) and southern polar cap (at Vostok in Antarctica), respectively. As the PC indices are used to estimate the solar wind merging field [*Troshichev et al.*, 2006, and references therein], the PC index values have been adjusted to have the same units as E_m [mV/m]. For the new, unified PC indices that are used here, the calculation procedures of the northern and southern indices have been unified, and a larger data set is used for the derivation of the coefficients [*Troshichev et al.*, 2006]. The data used in the present work have been provided directly from the Danish Meteorological Institute (P. Stauning, personal communication, 2008).

2.5. DMSP Data

[10] The PC potential drop is derived from the DMSP F13 spacecraft. This satellite has a sun-synchronous circular polar orbit where the satellite track is aligned along the dawn-dusk meridian. The special sensor for ions, electrons, and scintillation (SSIES) provides measurements of the horizontal plasma flow and ion density at a rate of 6 samples per second. The electrostatic potential distribution is derived by integrating the E-field along the satellite track, using $E = -v \times B$, where v is the measured transverse ion drift velocity and B is the model geomagnetic field. With an orbit time of 1 h 42 min there are approximately 8 oval crossings for each substorm within the examined 6 h time frame around substorm onset, half of them in the southern and half of them in the Northern Hemisphere. The PC potential drop is here calculated as the difference between the maximum and minimum potential found over the polar passage. For the calculation, E-field and convection pattern are considered steady for time periods shorter than the polar cap crossing time of approximately 10 min. Variations on shorter timescales are neglected by forcing the potential to zero at 50 degrees magnetic latitude. The potential offset at the end point is symmetrically removed from the potential pattern [e.g., *Rich and Hairston*, 1994]. All events have been manually inspected, and events with erroneous potential patterns due to data dropouts (approximately 3% of all cases) have been removed.

3. Methodology

[11] The 390 pseudobreakups and 484 substorms of the *Kullen and Karlsson* [2004] study have been identified by

visual inspection of Northern Hemisphere images from the UV imager on Polar. The event list covers the time period between 1 December 1998 and 28 February 1999. Every substorm-like activity that can be discerned on Polar UV images has been taken into account, even those that appear on the dawnside or duskside part of the oval. Only intensifications on the dayside oval between 10 and 14 MLT are excluded. As expected, the large majority of all intensifications appear on the duskside of the oval. Only 13% and 15% of all events occur at midnight and on the dawnside of the oval, respectively. All 874 events have been classified either as substorms or pseudobreakups. A pseudobreakup is here defined as an auroral intensification that does not expand globally and that appears at least during part of its lifetime outside the substorm main phases. PBIs are not included, as these appear during the substorm expansion and its recovery phase. Only those breakups where a considerable expansion in the dawn-dusk direction and signs of recovery (erosion of the activated auroral region) can be discerned on Polar UVI have been classified as substorms. Note, the expected poleward motion of the substorm onset intensification cannot be detected due to the limited spatial resolution of 50 × 50 km of the imager, and thus cannot be used for substorm onset identification. In about 85% of all cases, the classification into pseudobreakups and substorms from visible inspection of the UV images is obvious. To get a complete coverage of all breakups that appeared during the 3 month period, even the remaining cases have been classified as pseudobreakups or substorms, but are clearly marked as ambiguous events. Substorm onset (start of a pseudobreakup) is defined as the point in time where an auroral intensification becomes for the first time clearly visible on Polar UV image sheets where UV images are plotted with a 4–6 min time resolution. The optically determined onset times are correct within that time limit, i.e., the real optical onset may have appeared up to 4–6 min earlier, but not later. Pseudobreakups are further classified as isolated, growth-phase and recovery pseudobreakups. All pseudobreakups appearing within 30 min before the next substorm onset are referred to as growth-phase pseudobreakups, while auroral intensifications that start at the very end or just after substorm recovery are classified as recovery pseudobreakups. The remaining events are considered as isolated pseudobreakups (by *Kullen and Karlsson* [2004] referred to as single pseudobreakups). More details of event selection criteria can be found in the report by *Kullen and Karlsson* [2004] and *Kullen et al.* [2009].

[12] Figure 1 shows examples of each pseudobreakup type: in the first, second and third row an isolated, a growth-phase and a recovery pseudobreakup are shown. The plots give a polar view over the high-latitude Northern Hemisphere, with MLT-CGLat (Magnetic Local Time versus Corrected Geomagnetic Latitude) coordinates overlaid on Polar UV images. In the first row, an isolated pseudobreakup appears on the 4th and 5th image at 68 degrees latitude on a very small and faint oval. In the second row, third image, a growth-phase pseudobreakup is visible in the premidnight region of a small oval at about 68 degrees latitude. In the fifth image, the pseudobreakup brightening has disappeared, in the sixth image the same spot brightens again (onset) and develops in the following images into a full-scale substorm. In the last row, the end of a very active substorm recovery is seen. In the first images, the nightside oval is broad and very bright. The activated oval region reaches to very high latitudes. From the third image on it is possible to discern an isolated intensification near the oval boundary at 72 degrees latitude which remains at its location at highest latitudes for a long time after the remaining oval has retreated to lower latitudes. This type of auroral intensification can be identified repeatedly at the end of active substorm recoveries. It always appears as a single brightening, and nearly always (94%) close to the poleward oval boundary [*Kullen and Karlsson*, 2004]. Although such an intensification often starts as a poleward boundary intensification during recovery, it lasts long after the substorm faded (up to 10–30 min). Thus, according to the definition given above (all auroral intensification appearing during at least part of their existence outside the substorm main phases are counted as pseudobreakups) this type of recovery brightening is referred to as a recovery pseudobreakups.

[13] For a detailed study of the solar wind influence on the occurrence of auroral breakups, 1 min resolution solar wind parameters and AE index data are examined up to 3 h before and after each breakup. Mainly IMF B_Z and solar wind merging electric field are analyzed here. Since decades it is known that the substorm evolution is strongly controlled by IMF B_Z [e.g., *Akasofu*, 1980]. The solar wind merging electric field $E_m = vB_T\sin^2(\Theta/2)$ (with v as solar wind velocity, B_T the transverse IMF component and Θ the IMF clockangle in the yz-plane) is the fraction of the solar wind electric field that is assumed to map to the polar cap during southward IMF conditions. Thus, it gives an estimate of the amount of energy transferred from the solar wind to the magnetosphere through direct driving [*Kan and Lee*, 1979].

[14] To investigate how much of the solar wind energy reaches the polar cap region in the ionosphere, E_m is compared to the polar cap (PC) potential drop and to the unified northern and southern polar cap (PC) indices. Both parameters are known to correlate well with E_m [*Troshichev and Andrezen*, 1985; *Reiff et al.*, 1981]. However, the comparison is not as straightforward as it seems: a strong correlation between E_m and PC potential drop exists only during southward IMF. The formation of a clear 2 cell convection pattern during southward IMF indicates that the cross polar cap potential drop corresponds in this case to the mapped solar wind E-field [*Lockwood et al.*, 2009], i.e., E_m maps along open field lines of the polar cap to ionospheric heights. Even for the unified PC indices, the correlation is much better during southward than during northward IMF [*Troshichev et al.*, 2006]. Both, the PC potential drop and the PC indices are not only influenced by E_m but also by the substorm evolution: *Reiff et al.* [1981] observed that the nightside PC potential drop correlates strongly with the AL index while the best correlation with E_m is found in the dayside part of the polar cap. *Janzhura et al.* [2007] showed that the winter PC index correlates better with the AE index than the (high-conductive) summer PC index, independent of the hemisphere.

4. Results

4.1. Relation Between Oval Size, Substorm Strength and Solar Wind Merging E-Field

[15] In Figure 2 the influence of the solar wind merging field E_m on the substorm strength is investigated. For each

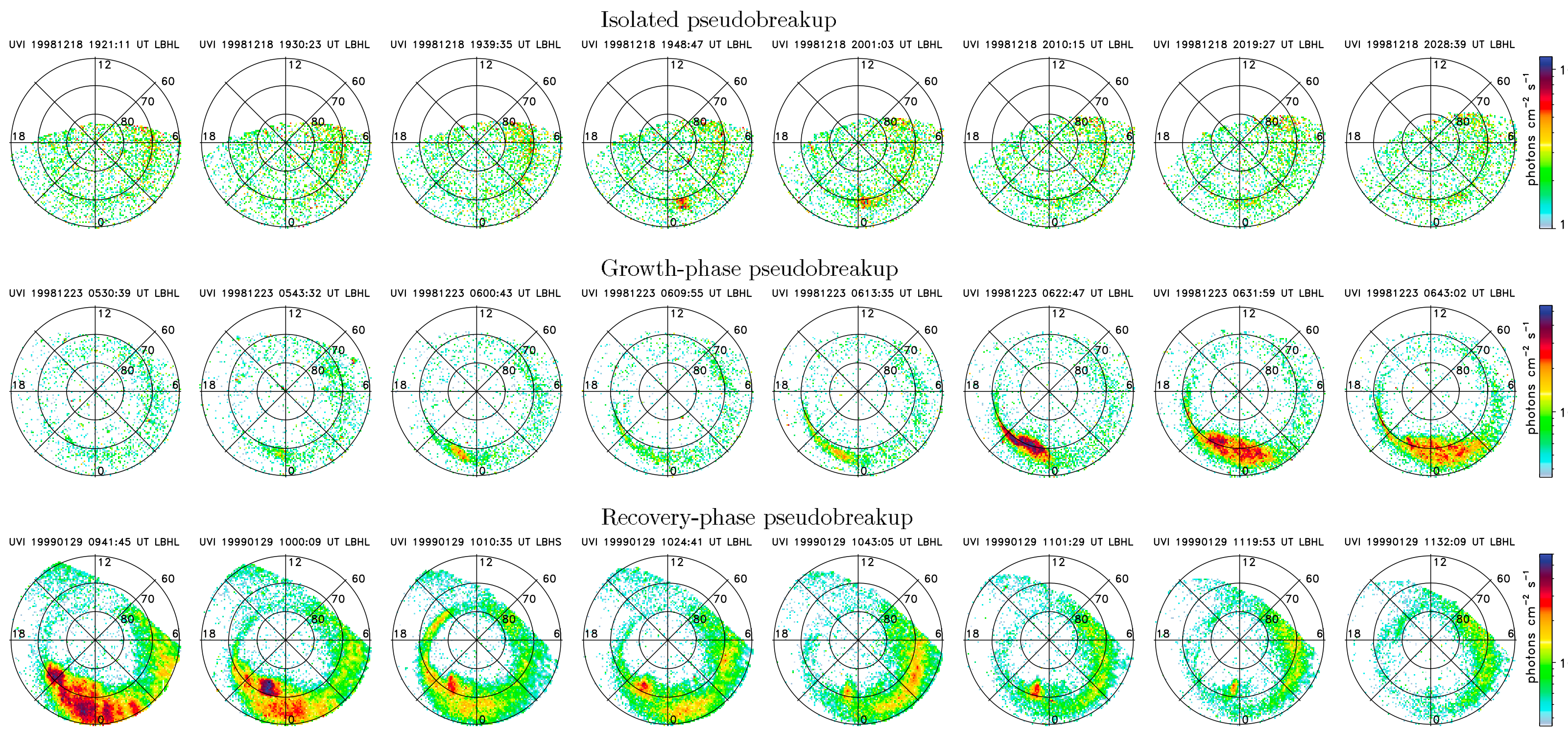

Figure 1. Examples of pseudobreakups seen on the Polar UV imager with the LBHL filter. The plots show a polar view of the Northern Hemisphere, with overlaid MLT-CGLat coordinates. In the top, middle and bottom rows, the temporal evolution of an isolated pseudobreakup, a growth-phase pseudobreakup, and a recovery pseudobreakup are shown, respectively.

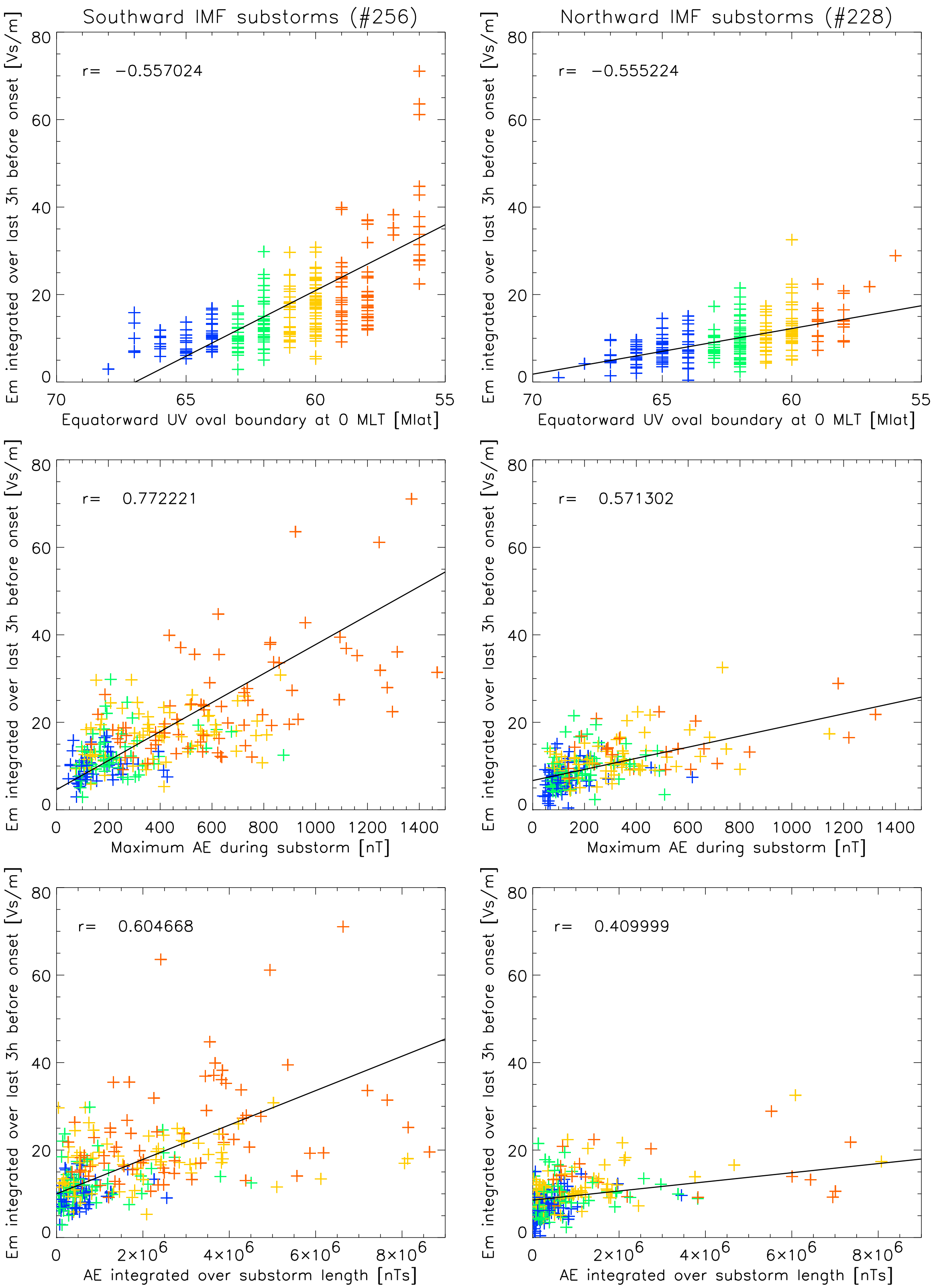

Figure 2. Solar wind merging E-field E_m integrated over the last 3 h before onset versus oval size (top plots), maximum AE value during substorm (middle plots), and AE integrated over the entire substorm (bottom plots). The left (right) column shows the results for all substorms with predominantly southward (northward) IMF during the last 3 h before onset. The crosses are color coded according to the location of the equatorward UV oval boundary at 0 MLT with blue (very small oval), green (small oval), yellow (medium oval) and red (large oval). Overlaid on the plots are the regression lines.

substorm, E_m values are integrated over the last 3 h before onset and are plotted versus the equatorward oval boundary location at 0 MLT at onset (Figure 2, top), versus the maximal AE index value during the substorm (Figure 2, middle) and versus AE values integrated over the entire substorm period (Figure 2, bottom). The substorms are separated by sign of IMF B_Z; the left column contains substorms with predominantly southward IMF during the last 3 h before onset, the right column substorms with predominantly northward IMF. As E_m gives an estimate for the energy transfer into the magnetosphere, the plots in Figure 2 show, how much the substorm strength depends on the energy loading during the last 3 hours before onset. The location of the equatorward UV oval boundary at 0 MLT is used as an indicator of the oval size (a further equatorward boundary location corresponds to a larger oval). To see how oval size and AE index are related, the crosses are color coded depending on the location of the equatorward oval boundary at 0 MLT. Boundary locations < = 60, between 60 and 62, between 62 and 63, and >64 CGLat are marked with red, yellow, green and blue colors, respectively. The boundaries are chosen such that each group contains approximately equally many substorms. The axis ranges are chosen such that nearly all events appear on the plots. In Figure 2 (left), 3 measurement points appear outside the y-axis. In Figure 2 (bottom left), 2 measurement points appear outside the x-axis.

[16] The correlations between integrated Em, substorm strength and oval size do not depend much on the chosen integration time. For the southward IMF cases the correlation coefficients change between an integration time of 30 min and 3 h from r = 0.52 to r = 0.56, from r = 0.74 to r = 0.77, and from r = 0.53 to r = 0.61 for oval size, AE max and integrated AE plots, respectively. For the northward IMF cases the correlation coefficients change more (r = 0.34–0.55, r = 0.39–0.57, r = 0.32–0.41 for oval size, AE max and integrated AE have highest values for a 2.5 h integration time with r = 0.65 and r = 0.47). However, even for the northward IMF plots the shapes of the distributions change very little for different integration times.

[17] As expected from the less efficient energy transfer during northward IMF, the northward IMF substorms are in general weaker (lower AE values) and appear on a smaller oval (more blue and green crosses) than southward IMF substorms. The lower angle of the regression line for the northward IMF substorms appears due to the dependence of E_m on the IMF clock angle, decreasing to zero for a pure northward IMF direction ($E_m = vB_T\sin^2(\Theta/2)$). In our data set there exist nearly as many substorms with predominantly northward IMF than predominantly southward IMF during the last 3 h before onset (for a 1 hour integration time this ratio decreases to one of three northward IMF substorms). In other statistical studies the number of northward IMF substorms is much lower. *Hsu and McPherron* [2003] found 10% events with exclusively northward IMF ±20 min around onset, for our data set the number is 28%, see *Kullen and Karlsson* [2004]). This discrepancy appears as very weak substorms (appearing in a majority during northward IMF) are only detected on global auroral images. Very weak substorms leave only weak or insignificant substorm signatures (see, e.g., AE index and tail dipolarization curves for the weakest substorms from *Kullen et al.* [2009]).

[18] The plots in Figure 2 (top) show that the oval size depends on how much energy has entered the magnetosphere the hours before onset. There is a lower limit for how small the oval may become for a certain value of integrated Em. The color coding of Figure 2 (middle) and 2 (bottom) confirms the expected correlation between oval size and substorm strength [*Feldsten and Starkov*, 1967]: most strong (weak) substorms appear on a wide (small) auroral oval. Thus, our estimate of the oval size (equatorward oval boundary at 0 MLT at onset) works fairly well as an indicator for the substorm strength. The equatorward oval boundary can also be taken as a proxy for the location of the inner (earthward) plasma sheet boundary, as the most equatorward auroral emissions coincide with the b2e boundary of DMSP data [*Kauristie et al.*, 1999]. Thus, the plots in the first row confirm that during active geomagnetic times (high integrated E_m values) the inner plasma sheet boundary moves earthward [*Lyons et al.*, 1999].

[19] Comparing the three rows in Figure 2 shows, the maximum AE value during substorms (Figure 2, middle) correlates best with the integrated E_m values, i.e., the maximum substorm strength depends strongly on the amount of solar wind energy transferred to the magnetosphere during the hours before onset. The plots with AE values integrated over the entire substorm time (Figure 2, bottom) show a similar distribution as the maximum AE plot (Figure 2, middle). However, the correlation is not as good as in the latter case. Substorm main phase and especially its often long recovery-phase depend not only on solar wind conditions before but also on solar wind conditions after onset. *Pulkkinen et al.* [2006] showed that the solar wind input during the substorm growth-phase mainly influences the first part of the substorm, and has much less influence on its recovery.

4.2. Solar Wind Energy Input Before Substorm Onset

[20] In Figure 3, the influence of the integrated solar wind merging field on regular substorms (Figure 3, top) is compared to its influence on pb substorms (Figure 3, middle). The last row shows integrated E_m values for growth-phase pseudobreakups (Figure 3, bottom). In Figure 3 (left), E_m is integrated for each event over the last 3 h before substorm onset (before pseudobreakup start) and is plotted versus the total time (in minutes) of southward IMF during these 3 h. In Figure 3 (right), E_m is integrated over the last time period of southward IMF before substorm onset (before pseudobreakup start). The x-axis gives the duration of the last southward time period before onset. The events with northward IMF at onset are not included in Figure 3 (right). This is the case for 33% regular substorms, for 35% pb substorms, and for 37% growth-phase pseudobreakups. The crosses are color coded in the same way as in Figure 2 according to the equatorward oval boundary location at onset and at pseudobreakup start, respectively (red, yellow, green and blue indicate large oval, medium oval, small oval and very small oval substorms). The squares in Figure 3 (bottom) mark those cases where the integrated E_m value before a pseudobreakup is larger than the integrated E_m value before the subsequent substorm.

[21] According to the loading-unloading substorm model [e.g., *Baker et al.*, 1995], during southward IMF energy

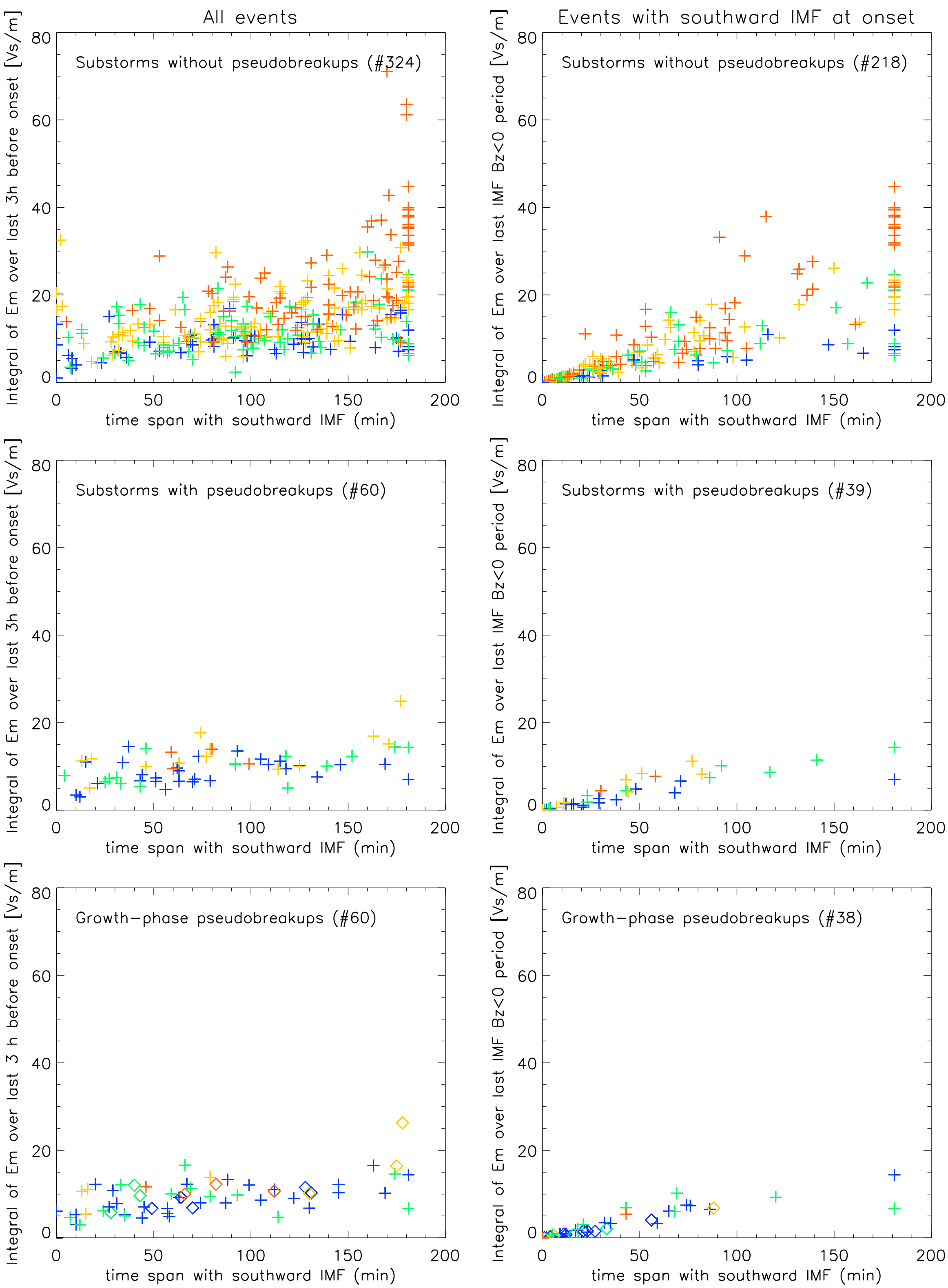

Figure 3. Solar wind merging E-field integrated over the last 3 h before onset (left column), and over the last southward IMF period before onset (right column) versus time period of southward IMF during integration time. The crosses are color coded, in the same way as in Figure 2, according to oval size. In the top, middle and bottom rows, the results are shown for regular substorms, pb substorms, and growth-phase pseudobreakups, respectively. The squares in the last plot mark all those events where the integrated E_m value before the pseudobreakup is larger than for the subsequent substorm.

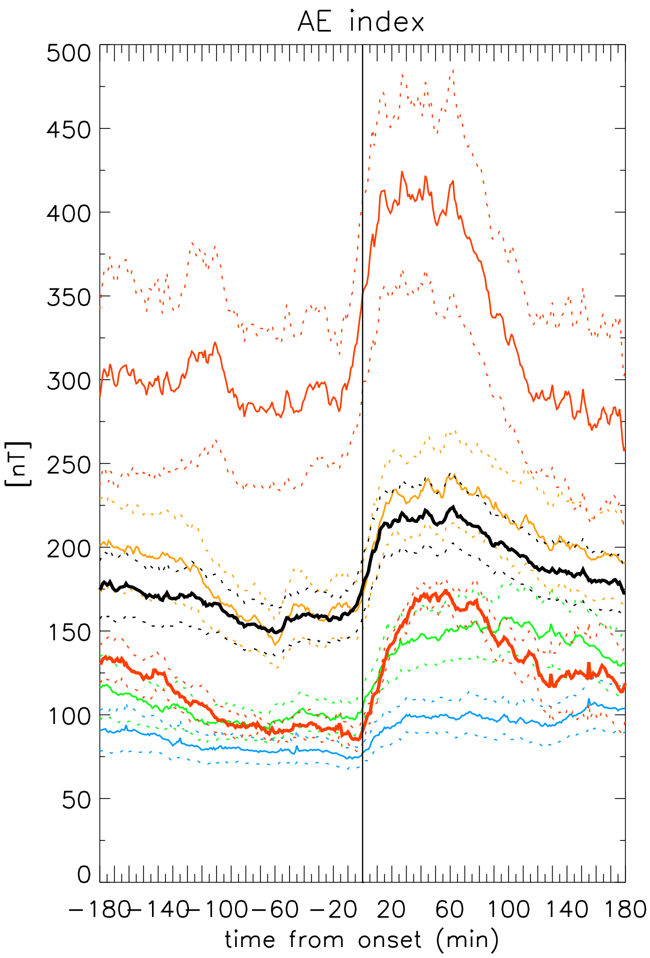

Figure 4. Superposed epoch curves of AE index up to ±3 h around substorm onset (vertical line). The thin red, yellow, green and blue curves give the average AE distribution for large, medium, small and very small substorms (categorized as in Figures 2 and 3 by oval size). The thick black and red curves show the average AE distribution for regular and for pb substorms, respectively. The correspondingly colored dotted curves show the 2-sigma deviation of the mean values.

loading of the magnetotail takes place via the addition of magnetic flux until the free energy is released via a substorm (unloading). In this context, the more interesting plots in Figure 3 are those where E_m is integrated over the last southward IMF period before onset (Figure 3, right). As about one third of all events disappear in Figure 3 (right), plots with a fixed 3 hour integration time have been produced where all events are included (Figure 3, left). A comparison between the left and right column in Figure 3 shows that the results do not depend much on whether the integration is done over the last 3 h before onset, or only over the last southward IMF period. Substorms preceded by pseudobreakups appear in a majority on a small or very small oval and the integrated E_m value is low. This holds even for the few events with extended southward IMF periods. In those cases the solar wind merging E-field is extremely low during a long time period. The threshold above which no pb substorms appear lies for southward IMF cases at 15 Vs/m (Figure 3, right). In case all events are taken into account and E_m is integrated over 3 h (Figure 3, left), this limit is exceeded in only 3 cases. All of these have values lower than 26 Vs/m.

[22] As expected from the short time span between growth-phase pseudobreakups and subsequent substorms, the plots for growth-phase pseudobreakups (Figure 3, bottom) show a similar distribution as the plots for pb substorms (Figure 3, middle) with nearly the same threshold values of 15 Vm/s and 27 Vm/s for southward and all cases, respectively. Comparing crosses and squares in Figure 3 (bottom) shows, in over two third of the cases the pseudobreakup has even lower integrated E_m values than the subsequent substorm.

[23] In opposite to pb substorms, regular substorms may appear for all levels of integrated E_m and oval sizes (Figure 3, top). The absence of a lower limit in integrated E_m of regular substorms means, not all weak substorms are preceded by growth-phase pseudobreakups. From a detailed analysis of Polar UV images from *Kullen and Karlsson* [2004] we know that there seems to be a smooth transition between the smallest auroral substorms and isolated pseudobreakups.

4.3. AE Index for Substorms of Different Strengths

[24] To study the time evolution of IMF B_Z, Em, AE, PCS and PCN around substorm onset, superposed epoch plots are produced. For each event, the data are centered around the optically determined auroral substorm onset. The analyzed solar wind parameter is plotted for each event with 1 min resolution up to 3 h before and after onset. The curves of all events are superposed on each other. For each minute, the average parameter value (from all events of the substorm subgroup in question) is calculated. Here, only these averaged curves of the superposed epoch plots are shown.

[25] In Figure 4, superposed epoch plots of the average AE distribution are shown for different substorm groups. As in Figures 2 and 3, the red, yellow, green, and blue curves correspond to the average AE distributions for substorm groups with an equatorward oval boundary at 0 MLT of less than 60°CGlat, 60–62°CGlat, 62–64°CGLat and above 64°CGlat, respectively. The thick black curve shows the average AE distribution for all regular substorms, the thick red curve (in the bottom part of the plots) shows the average AE distribution for all those substorms that are preceded by growth-phase pseudobreakups. The dotted curves give a 2 sigma deviation of the mean value, which corresponds to a 95% confidence interval of the mean value.

[26] Figure 4 shows, substorms with lower AE values (at onset and during the substorm) have on average a smaller oval size. With decreasing oval size the average AE shape is less pronounced. For the group of very small oval substorms only a weak AE increase and no clear AE decrease can be discerned. The average AE curve for regular substorms is similar to the curve for medium oval substorms. Pb substorms have in average as low AE index values as small and very small oval substorms. However, the shape of the AE curve for pb substorms differs significantly from weak substorms. Its AE curve is much more pronounced with a steep rise at onset and clear decrease of the AE index about 1.5 h later, indicating that most substorms with preceding growth-phase pseudobreakups are isolated substorms where the AE index reaches low values before a new substorm starts.

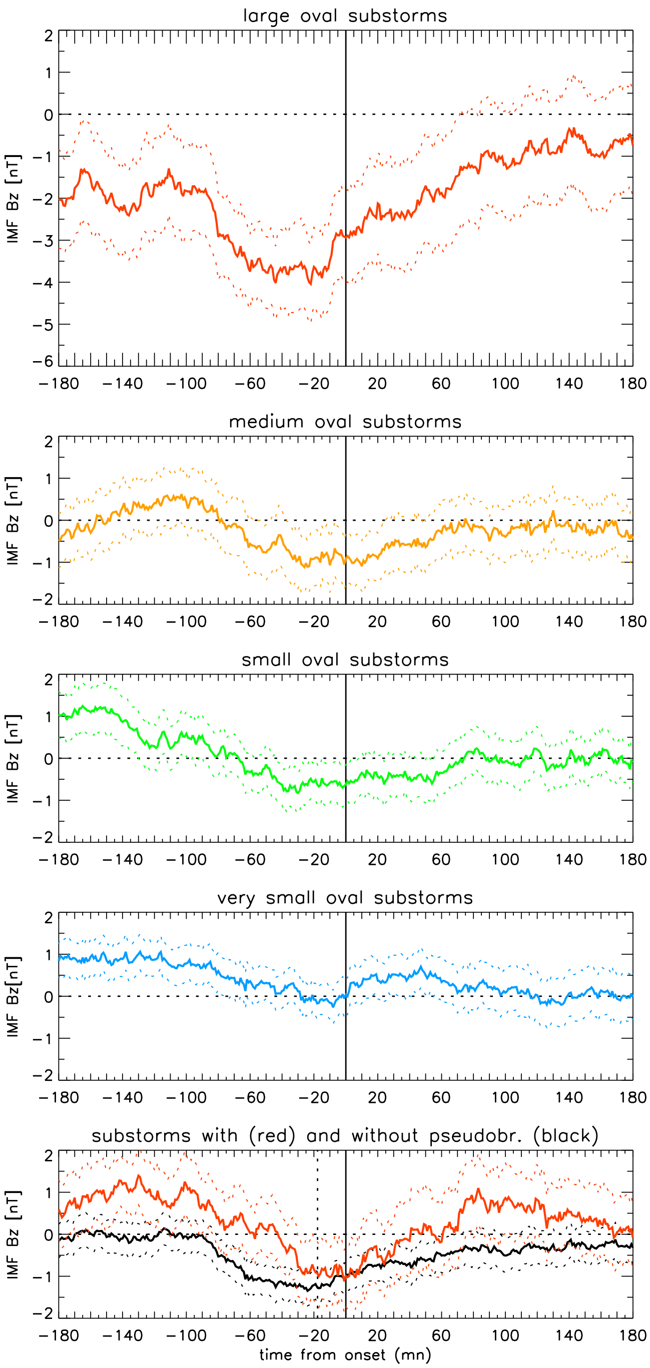

Figure 5. Superposed epoch curves of IMF B_Z up to ±3 h around substorm onset (plain vertical line). The first (top) to fourth panels show the results for large, medium, small, very small substorms. The bottom panel shows the IMF B_Z distribution for regular substorms (black) and pb substorms (red). The dotted vertical line in the bottom plot gives the average pseudobreakup start. The correspondingly colored dotted curves show the 2-sigma deviation of the mean values.

4.4. IMF B_Z for Substorms of Different Strengths

[27] In Figure 5, superposed epoch plots centered around substorm onset are shown for the IMF B_Z component. They are produced in the same way and the substorms are divided into the same subgroups as in Figure 4. The first four plots contain the average IMF B_Z distribution for substorms of decreasing oval size. In the bottom plot the average IMF B_Z curve for all regular substorms (black) and for pb substorms (red) are shown. The dotted lines in each plot give the 2 sigma deviation of the mean value.

[28] Figure 5 illustrates the well-known fact that substorms appear typically during periods of southward IMF. With decreasing substorm strength (as shown in Figure 4, the oval size correlates well with substorm strength) as the average time period and the magnitude of southward IMF decrease. Very small substorms commonly appear during IMF conditions with predominantly northward IMF. For this substorm group, onset is typically preceded by a short time period of extremely small negative IMF B_Z values.

[29] The average IMF B_Z distribution for regular substorms (Figure 5, bottom, red curve) confirms that a typical substorm starts after about 1–2 h southward IMF in accordance with the loading-unloading model [*Baker et al.*, 1995]. The average IMF values at onset for pb substorms have about the same magnitude as for regular substorms, although the former substorms are in general much weaker (lower AE values, see Figure 4). The main difference between the two substorm groups is the length of the southward IMF period before onset. Pb substorms appear typically after a much shorter southward IMF period which explains the smaller amount of magnetotail energy loading, leading to a weaker substorm. Note, the on average shorter southward period and the in average much lower energy loading in the hours before onset for pb substorms appear also in Figure 3. The strongly northward IMF values the hours before and after the short southward IMF period is a further indication that pb substorms appear often as isolated events during otherwise quiet times.

[30] Common for all substorm subgroups is that the average IMF B_Z curve starts to decrease to near zero or northward IMF values around substorm onset. The IMF B_Z decrease indicates that there exists a number of substorms that appear in connection with an IMF turn to northward IMF. Not all substorms appear after (an at least half hour long) loading during southward IMF [*Baker et al.*, 1995] but can be triggered immediately by sudden solar wind changes such as an IMF turn to northward B_Z, a strong IMF B_Y decrease or a sudden pressure jump. Each of these solar wind changes causes a reduction of the solar wind merging E-field and thus, a reduction of solar wind energy transfer to the magnetosphere which is assumed to be able to trigger the substorm onset [*Hsu and McPherron*, 2003].

[31] To check how many events of the present data set may be triggered, Table 1 gives the number of breakups that appear in connection with a northward IMF turning, an IMF B_Y decrease or a solar wind pressure jump. The substorms are divided into the same subgroups as in Figure 5. In the second column the number of substorms is given that have their onset close to an IMF northturn. An IMF northturn is defined here in two ways: on the left of column 2 the number of events is given (in percentage) for which IMF B_Z increases at least 2 nT from values below zero within ±10 min around onset. On the right (the number in parenthesis) the number of events is given that start within ±10 min of an IMF change from negative to positive. In the third column, the number of events is given that are not triggered by an IMF northward turning but for which an IMF $|B_Y|$ decrease of at least 2 nT

Table 1. Solar Wind Changes ±10 min Around Substorm Onset

Substorm Subgroup	B_Z Increase > = 2 nT (B_Z Sign Change)	$\|B_Y\|$ Decrease > = 2 nT if no B_Z Increase (if no B_Z Sign Change)	Pressure Change > = 7 nPa
Large substorms	58% (34%)	17% (32%)	1.0%
Medium substorms	50% (35%)	15% (22%)	0.0%
Small substorms	48% (50%)	11% (16%)	0.0%
Very small substorms	40% (43%)	14% (14%)	0.0%
Regular substorms	49% (40%)	14% (20%)	0.2%
Pb substorms	48% (48%)	18% (22%)	0.0%

appears within ±10 min around onset. The left (right values in paranthesis) give the number of IMF B_Y triggered events in case IMF B_Z has not increased of at least 2 nT (IMF B_Z has not changed sign). In the last column the number of events is given for which the solar wind pressure changes more than 7 nPa within ±10 min around onset (independent on whether it is an increase or decrease).

[32] The IMF conditions on the left of column 2 and 3 of Table 1 are chosen such that their results become comparable to the results of the statistical substorm study by *Hsu and McPherron* [2003]. Although the trigger requirements of Table 1 are less restrictive than in their study (requiring additionally a less than ±2 nT fluctuation ±20 min around the B_Z northward turning or B_Y decrease or a step-like pressure increase), the number of IMF triggered events is in our statistics comparable to their results: In the study by *Hsu and McPherron* [2003] 50% IMF B_Z triggered and 10% IMF B_Y triggered events are found, as compared to 49% and 14% IMF B_Z and B_Y triggered events in Table 1. Using the second northward turning definition (B_Z sign change, numbers in parenthesis), the numbers are 40% and 20% for IMF B_Z and B_Y triggered events, respectively. Both studies show that the number of events that appears in connection with a pressure change of more than 7 nPa are negligible (0.2% in our study, 1.5% in the study by *Hsu and McPherron* [2003]). Table 1 shows, that the only substorms that may be triggered by solar wind pressure jumps are large substorms. This can be expected, as a pressure jump appears commonly at the start of a magnetic storm.

[33] Comparing the different substorm subgroups with each other shows that the number of substorms connected to an IMF increase, increases with oval size (substorm strength). This may be explained in part by the larger fluctuations during periods with strong IMF (e.g., magnetic storms). Looking at the number of events with an IMF B_Z sign change to northward IMF (column 2, numbers in paranthesis), the opposite correlation occurs: small and very small substorms occur more often in connection with an IMF B_Z sign reversal than large or medium substorms. The reason is that most weak substorms have very small IMF B_Z values (Figure 5), thus even small fluctuations lead to IMF B_Z sign changes.

[34] The results for the IMF B_Y triggered events is strongly biased by which IMF B_Z trigger definition is chosen, i.e., which events are excluded from a check for an IMF B_Y decrease: For possible IMF B_Y triggered substorms where all IMF B_Z increase cases are excluded (3rd column left value): the different substorm groups have between 11% and 17% B_Y triggered cases. In case all IMF B_Z sign change cases are excluded (numbers in parenthesis) the number of B_Y triggered events increases with substorm strengh. No clear difference is found between substorms with and without growth-phase pseudobreakups, about half of all substorms in both groups may be triggered by an IMF B_Z northward turn and around one fifth by an IMF B_Y decrease.

4.5. Solar Wind Merging E-field and PC Index for Substorms With and Without Growth-Phase Pseudobreakups

[35] To find out about how much of the solar wind merging E-field reaches the high-latitude ionosphere, it is compared to the unified PC in Figure 6. The figure consists of superposed epoch plots centered around substorm onset showing E_m (green), unified PCN index (red) and unified PCS index (blue). To be able to put the results in context with the substorm evolution, the average AE index curve (black) is overlaid on the plots. For an easier comparison with the PC indices, AE is in each plot multiplied with a factor that is chosen such that the PCN curve overlaps during the growth-phase with the AE index curve. The top and bottom plots of Figure 6 show these four parameters for regular and pb substorms, respectively. The plain vertical line marks substorm onset, the dotted vertical line in Figure 6 (bottom) the average time span between pseudobreakup start and substorm onset. The dotted curves show the 2 sigma standard deviation of the mean.

[36] The shape of the E_m curves in Figure 6 is mainly controlled by the IMF B_Z component, as can be seen by comparing E_m to the IMF B_Z curves of Figure 5. The E_m curves rise about 1–2 h before substorm onset for both substorm groups, which is connected to the start of the IMF B_Z decrease. The main difference between the two E_m curves lies in the on average much lower values and the shorter time period of maximal E_m values before onset (30 instead of 60 min) for pb substorms.

[37] A comparison between E_m and unified PC index values in Figure 6 (top) shows that in average, E_m and PC index values are of the same order of magnitude with in average about 20% higher E_m than PC index values. During the substorm growth-phase, average E_m is much higher while during the main substorm phase, PC indices and E_m curves have similar values. Only in the summer hemisphere the PC index (in our study PCS) correlates well with the solar wind merging field, while the winter hemisphere PC (in our study PCN) index is strongly influenced by the AE index. During substorm expansion and recovery, both PC indices follow the AE curve more closely than the E_m curve. The connection between AE and PC indices has been observed by *Janzhura et al.* [2007] for isolated substorms. The present results show that this is valid in general. Note, the better correlation of PCN with AE does not appear because PCN measurements are taken in the same hemisphere as the AE index. As *Janzhura et al.* [2007] showed convincingly, the winter

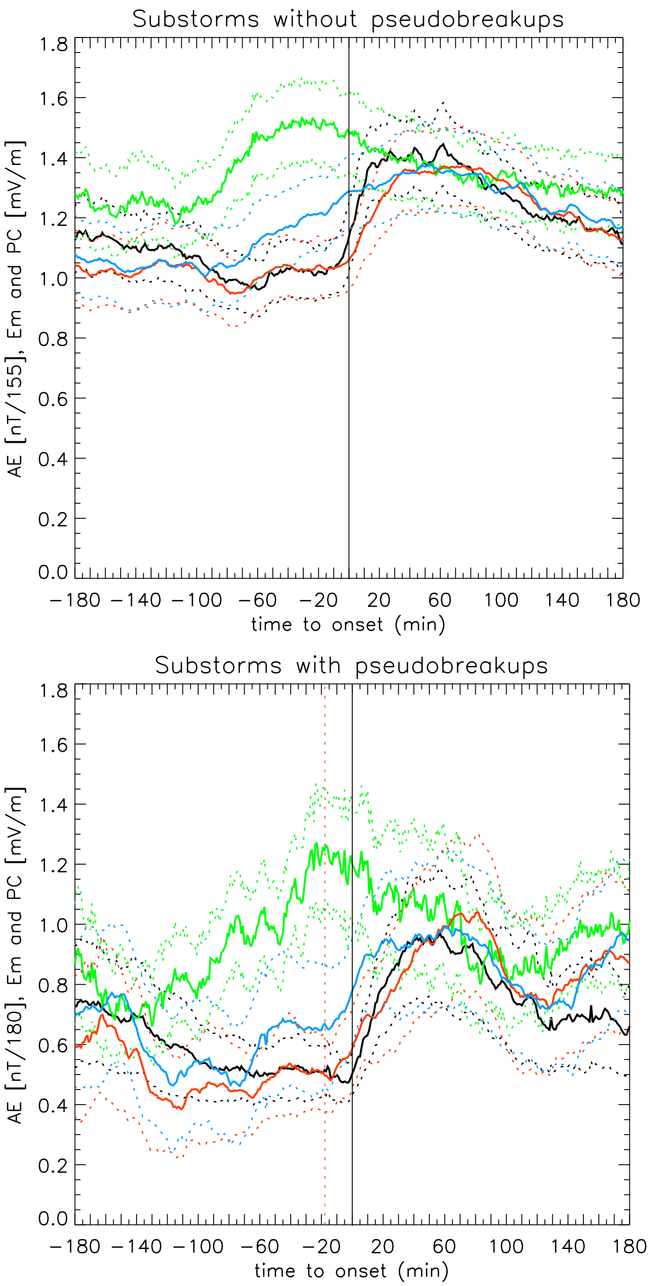

Figure 6. Superposed epoch curves of E_m, AE and PC indices for regular (top panel) and pb substorms (bottom panel) up to ±3 h around substorm onset (vertical line). The green, black, red and blue curves correspond to the average distribution of solar wind merging field E_m, AE index, unified PCN and PCS index. The correspondingly colored dotted curves show the 2-sigma deviation of the mean values.

PC index always correlates better with AE than the high-conductive summer index, independent of the hemisphere.

[38] Comparing the PC indices in the top and bottom plots of Figure 6 with each other shows that they are quite similar except for the generally much lower values of the PC indices for pb substorms. Even in Figure 6 (bottom), PCS approximately follows the E_m curve while PCN more closely follows the AE curve. Both curves are most closely aligned during the substorm main phase. The only deviation from the expected PC curve appears close to the (average) starting time of the growth-phase pseudobreakup. Both PCN and PCS begin to increase simultaneously during the pseudobreakup (i.e., even PCN increases before substorm onset). This indicates that the occurrence of a growth-phase pseudobreakup not only affects the auroral region but also latitudes poleward of the oval.

4.6. Polar Cap Potential Drop for Substorms With and Without Growth-Phase Pseudobreakups

[39] Another parameter to estimate how much of E_m reaches the high-latitude ionosphere is the PC potential drop [e.g., *Lockwood et al.*, 2009, and references therein]. Figure 7 summarizes the results for this parameter. The plots give the temporal evolution of the average potential drop up to 3 h before and after substorm onset (vertical line). Figure 7 (left) shows the average potential drop for regular substorms, Figure 7 (right) for pb substorms. Figures 7 (top), 7 (middle), and 7 (bottom) consist of plots for the average potential drop over the dayside polar cap close to the cusp (dayside DMSP passes below 83 deg magnetic latitude), at highest latitudes (DMSP passes above 86 degrees latitude), and near the nightside oval (nightside DMSP passes below 83 deg magnetic latitude), respectively. The spacecraft trajectory is such that all DMSP passes in the nightside group occur in the Southern Hemisphere, and all dayside events occur in the Northern Hemisphere. The averaging is done by a moving average filter with a window containing a fixed number of data points. A larger window (more data points) leads to a smoother curve and a decreased uncertainty of the mean value, which makes it easier to detect significant changes in the potential, however it increases the temporal uncertainty as the data points used for averaging will have a larger spread in time. For the left column a window of 50 data points is chosen. Due to the smaller number of data points in the right column, a smaller window has been used (20 data points). The gray curves give a 2 sigma deviation of the mean value.

[40] A strong increase of the potential drop magnitude can be discerned in all plots. There is a clear time shift between dayside (Figure 7, top) and nightside plots (Figure 7, bottom) regarding the start of the increase. The average dayside potential drop increases about an hour before substorm onset in both columns, while the average nightside potential drop increases at (40 min after) substorm onset in Figure 7 (left) (Figure 7, right). This time shift is expected, as the dayside potential drop is strongly controlled by the solar wind merging E-field [e.g., *Reiff et al.*, 1981] which increases 1–2 h before onset (Figure 6), while the nightside potential drop is mainly influenced by the substorm evolution [*Lockwood et al.*, 2009, and references therein].

[41] The dayside potential drop curves in the left and right columns resemble the solar wind merging E-field curves (Figure 6) with a long (short) time span of enhanced potential drop values (above 30 kV) for substorms without (with) growth-phase pseudobreakups. The nightside potential drop increases for the group of regular substorms exactly at onset, and about 40 min later for pb substorms. This corresponds roughly to the shape of the average AE curves, having their maxima 15 min and 40 min after onset for the substorms without and with growth-phase pseudobreakup groups, respectively (Figure 6). The much later potential drop increase for pb substorms is probably connected to the slow start of substorm expansion after pseudobreakups. For

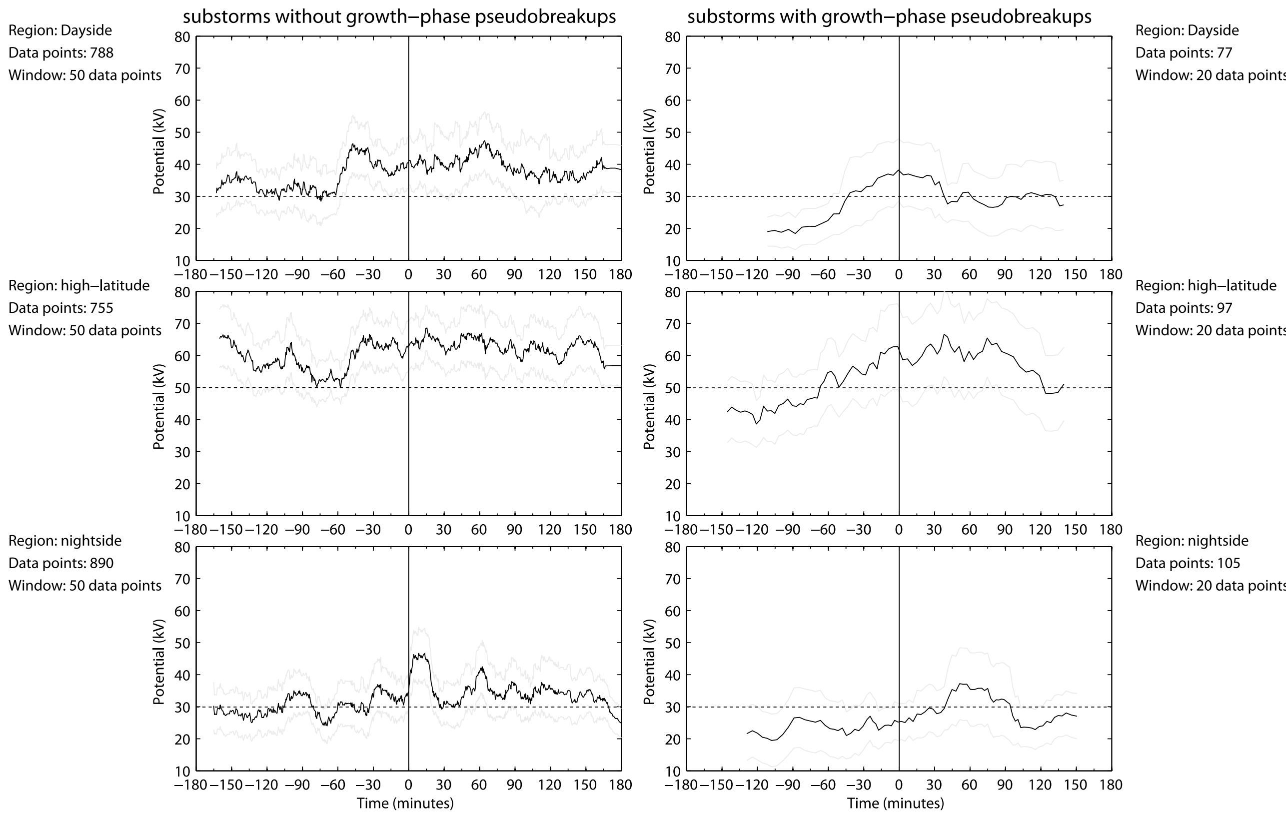

Figure 7. The temporal evolution of the average polar cap potential drop values around substorm onset of regular substorms (left column) and pb substorms (right column). The polar cap potential drop is calculated for all DMSP passes within ±3 h around substorm onset, resulting in about 8 data points for each event. The potential drop values are averaged each minute over the closest 50 (20) datapoints in the left (right) column. The top, middle and bottom panels show the average polar cap potential drop curves for dayside (<83 deg lat), high-latitude (>86 deg lat) and nightside DMSP passes (<83 deg lat), respectively. The gray curves give a 2-sigma deviation of the mean value.

examples *Kullen et al.* [2009] observed a commonly weak luminosity and slow expansion of the intensified auroral region during the first part of the expansion phase of pb substorms.

[42] For the high-latitude DMSP passes (middle plots) the potential drop values can be taken as an estimate of the total cross polar cap potential in cases where a clear 2 cell convection pattern appears. This is typically the case during southward IMF conditions [e.g., *Heelis*, 1984; *Heppner and Maynard*, 1987]. The shapes of the curves are influenced by both E_m and the substorm evolution, thus the pattern is much less pronounced than in the other plots. The maximal high-latitude potential drop values are about the same for both substorm groups. A level of 60–70 kV corresponds to typical cross polar cap potential values during southward IMF [*Sundberg et al.*, 2008]. During the hours before and after the substorm the high-latitude potential drop values are lower for pb substorms (39–48 kV instead of 50–66 kV for regular substorms), reflecting the fact that pseudobreakups appear mainly before isolated substorms. As regular substorms appear often during extended time periods with recurrent substorms [*Kullen and Karlsson*, 2004] and high geomagnetic activity level (see Figure 4), the average cross polar potential values are high even the hours before and after the substorm for this substorm group.

[43] A test with different averaging window sizes shows that the relative time shifts between dayside and nightside plots as well as the differences between the two substorm groups, described above, are independent of the chosen window size. The choice of the limits in latitude for dayside and nightside plots influence the results as well. The increased polar cap potential drop values around onset in the nightside (bottom) plots are mainly caused by a few data points close to the auroral oval where the visible part of the substorm takes place. Above 85 degrees latitude mixed dayside-nightside signatures are seen, i.e., several small increases are seen before as well as after onset.

4.7. Solar Wind and Ionospheric Parameters for Different Types of Pseudobreakups

[44] In Figure 8, solar wind and ionospheric parameter distributions for the three different pseudobreakup types are compared to each other. It contains the temporal evolution of average AE index, PCN, PCS, E_m and IMF B_Z. The black, red and blue curves correspond to the average curves of the superposed epoch plots for isolated, growth-phase, and recovery-phase pseudobreakups, respectively. The (average) starting time of pseudobreakups is marked with vertical dotted lines, for substorm onset with vertical plain lines. In the first AE plot (top panel) all events are centered around

the starting time of the pseudobreakups (dotted line). It includes 226 isolated pseudobreakups, 60 growth-phase pseudobreakups (only the last one before onset is counted), and 98 recovery-phase pseudobreakups. The remaining plots in Figure 8 are centered around the onset of the subsequent substorm. In these plots, only those recovery and isolated pseudobreakups that are directly followed by a substorm are taken into account (i.e., no other pseudobreakup appears between the studied event and the next substorm). This reduces the number of isolated and recovery pseudobreakups to 29 and 71 events, respectively.

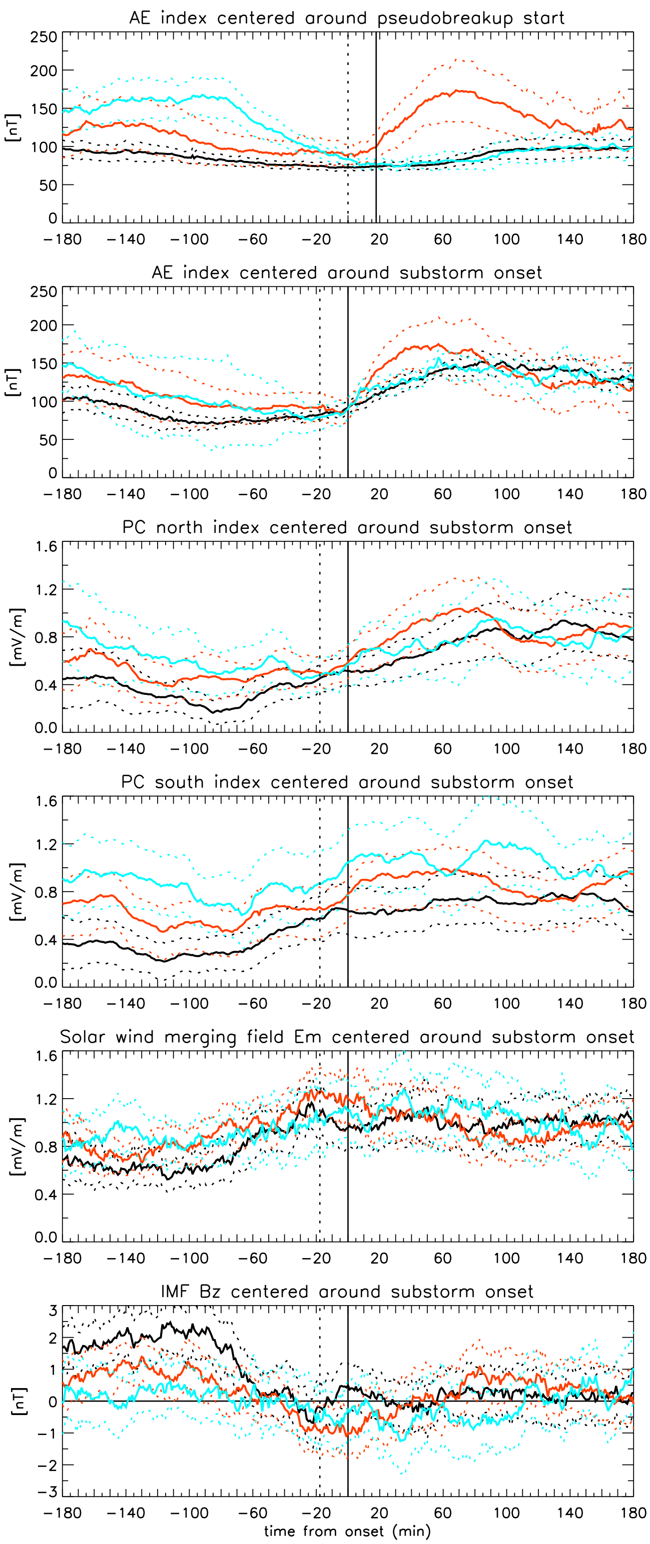

[45] Figure 8 (top) shows, as expected from the selection criteria for the different pseudobreakup types, growth-phase pseudobreakups appear in general about 10–20 min before the begin of a steep AE increase, recovery-phase pseudobreakups at the very end of an AE decrease and isolated pseudobreakups during an extended period of very low AE values, indicating the absence of substorm activity. There is no AE signature in the average AE curves which appears in connection with the pseudobreakup start. Although growth-phase pseudobreakups appearing before strong substorms may cause small bumps in the corresponding AE curve (see examples from *Kullen et al.* [2009]), these cases are rare. The reason is that all three pseudobreakup types appear on average on a very small oval. Of all pseudobreakups studied in this work, two thirds (one third) appear when the equatorward oval boundary is at 63 CGLat (66 CGLat) or higher. The average equatorward oval boundary for isolated, growth-phase and recovery pseudobreakups is at 0 MLT 64.6 CGlat, 63.8 CGlat, and 64.1 CGlat, respectively. Thus, not only recovery pseudobreakups, that start typically as poleward boundary intensifications, but even isolated and growth-phase pseudobreakups occur at high latitudes, although 65%–80% of these are not located at the poleward oval boundary. Of 12 AE stations, situated between 60.4 and 71.2°C Glat, only 5 stations are at 68°C Glat or higher. Thus, the possibility that a localized brightening at highest latitudes leaves a clear signature in the AE curve is rather small.

[46] Interestingly, the average AE curves for the three pseudobreakup types have similar AE values at pseudobreakup start (72 nT ± 30 nT, 89 nT ± 57 nT, and 84 nT ± 34 nT for isolated, growth-phase and recovery-phase pseudobreakups, ± gives the standard deviation). Comparing these values with AE values at onset for the different substorm groups in Figure 4 shows that pseudobreakups appear on average for AE values that are comparable to those during very small substorms.

[47] The second panel in Figure 8 shows that the same holds for the average AE curves centered around substorm onset. The three curves overlap around onset of the first substorm after a pseudobreakup (the average onset values are 92 nT ± 27 nT, 91 nT ± 57 nT and 90 nT ± 36 nT for isolated, growth-phase and recovery pseudobreakups). Usually the first substorm onset after a pseudobreakup appears on an oval with low AE values, independent of how long after the pseudobreakup the substorm starts. The onset values are

Figure 8. Superposed epoch curves of growth-phase pseudobreakups (red), recovery pseudobreakups (blue) and isolated pseudobreakups (black), centered around substorm onset (top panel) and pseudobreakup start (2nd to 5th panels). The plain curves give the average parameter value up to ±3 h around substorm onset, the correspondingly colored dotted curves the 2-sigma deviation of the mean value. The vertical plain and dotted lines mark substorm onset and pseudobreakup start, respectively. The plots show (from top to bottom) AE index (centered around pseudobreakup start), AE index (centered around onset), unified PCN index, unified PCS index, Em-field and IMF B_Z.

Table 2. Solar Wind Changes ±10 min Around Pseudobreakup Start

Substorm Subgroup	B_Z Increase > = 2 nT (B_Z Sign Change)	$\lvert B_Y \rvert$ Decrease > = 2 nT if no B_Z Increase (if no B_Z Sign Change)	Pressure Change > = 7nPa
Growth pseudobreakups	48% (37%)	17% (25%)	0.0%
Isolated pseudobreakups	22% (32%)	24% (23%)	0.0%
Recovery pseudobreakups	26% (35%)	24% (21%)	0.0%
Regular substorms	49% (40%)	14% (20%)	0.2%

comparable to those of small substorms (see Figure 4). Even the hours before and after onset the AE curves for the three different pseudobreakup types have a very similar shape.

[48] The remaining plots (lower three panels) show a similar temporal evolution of all three curves even for PC indices and solar wind drivers. As expected from the strong correlation between winter PC index and AE index [*Janzhura et al.*, 2007], the three PCN curves have similar values close to substorm onset. In the PCS curve, the values deviate more. The similar shapes of the different E_m curves as well as similarities in the IMF B_Z curves (IMF turns southward on average between 45 and 35 min before substorm onset) shows that the average solar wind conditions leading to the onset of the first substorm after a pseudobreakup are comparable, although the time span between pseudobreakup and substorm varies largely between the different pseudobreakup types. On average, growth-phase pseudobreakups appear 18 min, isolated pseudobreakups 120 min and recovery pseudobreakups 177 min before the next substorm. These results indicate that there exists a characteristic set of solar wind conditions that are favorable for the first substorm after a pseudobreakup to develop.

[49] To find out about possible solar wind triggers of pseudobreakups, Table 2 shows the number of pseudobreakups that may be triggered by a northward turning of the IMF, IMF B_Y decrease or a solar wind pressure jump. As in Table 1, the second column gives the number of events where IMF B_Z is increasing of at least 2 nT from a southward IMF value within ±10 min from an IMF B_Z turn. In parenthesis the number of events is given that appear close to an IMF B_Z sign reversal from negative to positive. The third column lists all events that do not involve an IMF B_Z northward turning, but an IMF B_Y decrease of at least 2 nT. The last column gives the number of events which appear close to a pressure change of at least 7 nPa. The results are listed for each pseudobreakup group. For an easier comparison the results for regular substorms (Table 1) are repeated in the last row.

[50] Table 2 shows a clear difference between growth-phase pseudobreakups and the other two pseudobreakup types regarding the number of events connected to a clear IMF B_Z increase. While growth-phase pseudobreakups are as often triggered by IMF B_Z as substorms, single and recovery pseudobreakups appear less often in connection with an IMF B_Z increase. Looking at the number of IMF B_Z sign change cases, this difference is nearly smeared out. No pseudobreakup occurs close to a sudden pressure jump. The number of single and recovery pseudobreakup events connected to clear B_Y decreases (incase no B_Z increase occurs) is higher than for substorms. However, this result is strongly biased by the fact that more of these pseudobreakup events are checked for an IMF B_Y decrease than growth-phase pseudobreakups and substorms (as their number of IMF northward turning events is smaller). The results in Table 2 show, it is not very probable that recovery or isolated pseudobreakups are triggered by sudden solar wind or IMF changes, while growth-phase pseudobreakups may very well be caused by an IMF B_Z increase.

5. Discussion

[51] In this work we examine solar wind conditions and ionospheric response during 390 pseudobreakups and 484 substorms, identified from global auroral images from Polar UVI during three winter months in 1998/99. The goal is to investigate why sometimes pseudobreakups appear during the growth-phase of a substorm (pb substorm) and sometimes they do not (regular substorm). To find out possible differences between substorms that are preceded by growth-phase pseudobreakups (pb substorms) and substorms without growth phase pseudobreakups (regular substorms), solar wind and ionospheric conditions of pb substorms are compared with those of regular substorms. In addition we compare growth-phase pseudobreakups to isolated pseudobreakups and to recovery pseudobreakups.

[52] The solar wind energy is by many researchers assumed to be responsible for whether an auroral intensification develops into a global substorm or not [e.g., *Nakamura et al.*, 1994; *Partamies et al.*, 2003, and references therein]. To investigate that, the solar wind merging field is examined in detail as it gives a good estimate of the solar wind energy transfer into the magnetosphere. The unified northern and southern PC indices and the PC potential drop (derived from DMSP data), are analyzed to find out how much of E_m reaches the polar cap region of the ionosphere. Both parameters are known to correlate well with E_m [*Lockwood et al.*, 2009; *Troshichev et al.*, 2006]. The response in the auroral zone is studied using UV images from the Polar spacecraft and the AE index.

[53] Although the superposed epoch analysis plots in Figures 4–7 are derived from independent data sets (OMNI solar wind data, DMSP PC potential plots, PC indices, and AE index) they all show the same tendency regarding the difference between pb and regular substorms. This gives us reason to trust the average curves for the different parameters that have been derived using the superposed epoch analysis around substorm onset. The entire coupling process between solar wind energy, its transfer to the magnetosphere, the response from the high-latitude ionosphere (PC index and PC potential drop), and the effect on auroral substorms can be followed from the resulting plots.

5.1. Solar Wind Influence on Substorms With Growth-Phase Pseudobreakups

[54] From our previous work [*Kullen and Karlsson*, 2004] we were able to show that IMF magnitude, solar wind

velocity, absolute value of IMF B_Z, and the epsilon parameter (E_m gives nearly identical results as epsilon) have in average much lower values during pseudobreakups than during substorms. However, in the study from 2004 [*Kullen and Karlsson*, 2004], we were not able to find a critical limit for any of these parameters above which pseudobreakups or below which regular substorms disappear completely.

[55] The main result of the present study is the discovery of such a common threshold. We found a solar wind parameter which provides a limit above which growth-phase pseudobreakups and subsequent substorms do not appear. According to the loading-unloading model, energy is stored in the magnetosphere through the addition of open flux during southward IMF until it is released via a substorm [e.g., *Baker et al.*, 1995]. Here, the energy which has entered the magnetotail since the last IMF southward turning, is estimated by integrating E_m over the last southward IMF period before pseudobreakup start (substorm onset). Figure 3 (right) shows there exists an upper limit of integrated E_m values (15 Vs/m) above which growth-phase pseudobreakups and subsequent substorms (pb substorms) disappear completely. In other words, growth-phase pseudobreakups and subsequent substorms do not occur when the accumulated solar wind energy in the magnetosphere becomes too high.

[56] The energy threshold found here is a necessary, but not a sufficient condition for pb substorms to occur. Many of the substorms appearing after low integrated Em values have no growth-phase pseudobreakups. Figure 3, upper row shows, regular substorms may appear for a large range of integrated E_m values. Neither a lower nor an upper limit is found below or above which regular substorms disappear completely. This result and the results from the examination of the AE index curves (Figures 4 and 8) and evolution of auroral substorms on global aural images [*Kullen and Karlsson*, 2004] confirm what has been suggested by several researchers before [e.g., *Aikio et al.*, 1999, and references therein]: there is a continuous transition between weakest auroral intensifications (isolated pseudobreakups) and substorms of increasing strength.

[57] Nearly half of all substorms in this study appear during predominantly northward IMF. The unusually high number of northward IMF events as compared to other studies is due to the selection by visual inspection of UV images. Thus even weakest substorms are taken into account, which are more likely to occur during northward IMF. It is known that a transfer of solar wind energy into the magnetosphere takes place even during northward IMF [e.g., *Crooker*, 1992], though with a lower transfer rate (E_m depends on $\sin^2(\Theta/2)$). To test whether the above results hold also for northward IMF substorms, E_m has been integrated over the last 3 hours before onset (a shorter integration time changes the results only marginally), independent on the sign of IMF B_Z. These plots (Figure 3, left) give qualitatively the same results as the plots where only the last southward IMF period has been taken into account (in only 5% of the cases, the values exceed the threshold for southward IMF cases of 15 Vs/m).

[58] In summary, pb substorms occur only when the accumulated solar wind energy does not exceed a certain threshold. However, not all substorms that start after only a small amount of solar wind energy has reached the magnetosphere, are preceded by growth-phase pseudobreakups. As can be seen from the AE plots in Figure 4, pb substorms have in average a strength comparable to small and very small substorms. The difference between a typical pb substorm and small (very small) regular substorms lies in the more abrupt change between clearly northward to clearly southward IMF (Figure 5) for a typical pb substorm, as well as a more pronounced AE shape of the substorm (steeper rise and fall of AE and a shorter time period of maximal AE values) (Figure 4). The latter indicates a more defined substorm evolution with clear expansion and a short recovery as compared to regular substorms of the same strength.

[59] An investigation whether pb substorms are systematically triggered by an IMF northward turning (Table 1) does not show any difference between these and regular substorms. In both substorm groups, about half of all substorm onsets appear in connection with an IMF B_Z northward turning (strong increase). The same holds for growth-phase pseudobreakups. In opposite, for isolated or recovery pseudobreakups, a much smaller number of cases with a strong IMF B_Z increase is found (Table 2), indicating that these are probably not triggered by IMF B_Z changes. The number of substorms and pseudobreakups that are not connected to an IMF B_Z change, but with an IMF B_Y decrease is not very high for any substorm or pseudobreakup subgroup (less than one forth of all events). A check for events that may be caused by sudden pressure pulses shows that no pseudobreakup and only 0.2% of all substorms are triggered by these. All pressure pulse triggered substorms to the group of large substorms (commonly the first substorm after a CME event has reached the Earth bow shock).

[60] Other solar wind parameters such as the solar wind velocity, density and pressure have been investigated for a possible influence on different substorm groups. The results are not shown here, as these parameters in most cases do not change much during the hours before and after onset. Already known from *Kullen and Karlsson* [2004] is that substorms of increasing strength appear for increasingly higher (lower) solar wind velocity (density). The velocity, density and pressure plots for pb substorms resemble those of small and very small substorms.

5.2. Ionospheric Response During Substorms With Pseudobreakups

[61] The difficulty with determining how much of E_m has reached the high-latitude ionosphere is that both the PC index and PC potential drop are influenced not only by E_m but also by magnetosphere-ionosphere coupling processes during substorm expansion. Summer PC index during the growth phase [*Janzhura et al.*, 2007] and dayside PC potential drop [*Lockwood et al.*, 2009] have been shown to correlate best with E_m, while winter PC index and nightside PC potential drop are mainly influenced by the AE and AL indices, respectively. This behavior is confirmed in the present study (Figures 6 and 7).

[62] The most important result shown in Figure 6 is that both the average E_m and average PC index curves have very low values for pb substorms as compared to regular substorms. The low solar wind energy transfer rate for average pb substorms is directly mirrored in the low PC index values. The values during the main phase of pb substorms are at

the same level as the minimum values (before the growth-phase begins) of regular substorms. However, the difference between smallest and highest E_m (and PC index) values (before growth phase and at maximal AE values) is larger for pb substorms than for regular substorms. Possibly such a strong increase of the energy transfer is necessary to trigger the first substorm after quiet times.

[63] Although less pronounced than in the PC index plots, even the cross polar cap potential drop curves differ between pb substorms and regular substorms (Figure 7, middle). The average cross polar cap potential drop is the hours before and after a substorm much lower for pb substorms (39–48 kV) than for regular substorms (50–66 kV), a further indication that pb substorms are typically isolated events.

[64] That a pb substorm appears often as the first substorm after a geomagnetically quiet period is indicated in several independent data sets of our study. The low level of average PC index and cross polar potential drop the hours before onset of a pb substorm is closely connected to the in average low solar wind energy transfer into the magnetosphere during this time period (Figure 6) which, in turn, is mainly influenced by the temporal evolution of IMF B_Z. Figure 5 shows typically northward solar wind conditions the hours before onset of a pb substorm. During such IMF conditions, the magnetosphere is mostly in a quiet state. As seen in Figure 4, the average AE index has very small values the hours before onset of a pb substorm, indicating there appears commonly no substorm activity the hours before a growth-phase pseudobreakup and the subsequent substorm appear.

[65] From the results by *Janzhura et al.* [2007], it is expected that the summer and winter PC index follow closely the average E_m and AE curves during the entire substorm growth phase, respectively. An interesting deviation from the expected shape of the PC index curves is found in the pb substorm plot of Figure 6: PCN and PCS indices increase simultaneously at the average start time of growth-phase pseudobreakup. This indicates that growth-phase pseudobreakups influence magnetic field variations in the polar caps of both hemispheres.

5.3. Comparison Between Growth-Phase, Isolated and Recovery Pseudobreakups

[66] Figure 8 shows an astonishing similarity between average AE, PC, B_Z and E_m curves for all three pseudobreakup types, although these occur by definition during different substorm phases. Also, the different pseudobreakups map to different regions in the magnetosphere depending on their location with respect to the latitudinal distribution of the oval. Most recovery and growth-phase pseudobreakups are known to appear at the poleward [*Kullen and Karlsson*, 2004], and equatorward oval boundary [e.g., *Aikio et al.*, 1999], respectively.

[67] Comparing the average distribution of solar wind parameters for the three different pseudobreakup groups with each other, we find that average IMF B_Z and the merging E-field, have a very similar temporal evolution the hours before the first substorm after a pseudobreakup, independent of whether it is a growth-phase, isolated or recovery-phase pseudobrekaup. This means, there exists a characteristic set of solar wind conditions for the first substorm appearing after a pseudobreakup, independent of how much time has passed since the last pseudobreakup appeared.

6. Summary

[68] In this work it is shown on a statistical basis that substorms preceded by growth-phase pseudobreakups appear only when the amount of energy transferred into the magnetosphere the hours before onset has not exceeded a certain limit. Predominantly northward IMF and an only short time of and/or weakly southward IMF the hours before onset are the cause. The low energy transfer into the magnetosphere is reflected by low PC index and cross PC potential values before and during pb substorms as compared to regular substorms. Low AE index values and small oval size before and even during pb substorms show that substorm preceded by growth-phase pseudobreakups are in average weak and appear typically after a quiet time period during which substorm activity is nearly absent. These results confirm what has been suggested by many authors before: the occurrence of growth-phase pseudobreakups is ultimately controlled by the solar wind energy transfer into the magnetosphere.

[69] **Acknowledgments.** We are grateful to P. Stauning for providing the unified PC index data. We thank the CDA Web and the GOES team for providing GOES data. We acknowledge G. Parks as the principal investigator for the Polar UV imager, the ACE, IMP-8, and Wind instrument teams for providing magnetometer and plasma data through the GSFC/SPDF OMNIWeb interface at http://omniweb.gsfc.nasa.gov. We thank the WDC-C2 Kyoto AE index service, the AE stations, and the persons who derive the index for access to AE index data on the Internet. Work at the University of Texas at Dallas was supported by NSF grant ATM0536868. We gratefully acknowledge the William B. Hanson Center for Space Sciences at the University of Texas at Dallas for providing the DMSP thermal plasma data.

[70] Robert Lysak thanks Victor Sergeev and Gordon Rostoker for their assistance in evaluating this paper.

References

Aikio, A. T., V. A. Sergeev, M. A. Shukhtina, L. I. Vagina, V. Angelopoulos, and G. D. Reeves (1999), Characteristics of pseudobreakups and substorms observed in the ionosphere, at geosynchronous orbit, and in the midtail, *J. Geophys. Res.*, *104*, 12,263, doi:10.1029/1999JA900118.

Akasofu, S.-I. (1980), The solar wind-magnetosphere energy coupling and magnetospheric disturbances, *Planet. Space Sci.*, *28*, 495, doi:10.1016/0032-0633(80)90031-8.

Baker, D. N., A. J. Klimas, and D. V. Vassiliadis (1995), Energy transfer between the solar wind and the magnetosphere-ionosphere system, *J. Geomag. Geoelectr.*, *47*, 1171.

Crooker, N. U. (1992), Reverse convection, *J. Geophys. Res.*, *97*, 19,363, doi:10.1029/92JA01532.

Elvey, C. T. (1957), Problems of auroral morphology, *Proc. Natl. Acad. Sci. U. S. A.*, *43*, 63, doi:10.1073/pnas.43.1.63.

Feldsten, Y. I., and G. V. Starkov (1967), Dynamics of auroral belt and polar geomagnetic disturbances, *Planet. Space Sci.*, *15*, 209, doi:10.1016/0032-0633(67)90190-0.

Fillingim, M., et al. (2000), Coincident POLAR/UVI and WIND observations of pseudobreakups, *Geophys. Res. Lett.*, *27*, 1379, doi:10.1029/1999GL010773.

Heelis, R. (1984), The effects of interplanetary magnetic field orientation on dayside high-latitude ionospheric convection, *J. Geophys. Res.*, *89*, 2873–2880, doi:10.1029/JA089iA05p02873.

Henderson, M. G., G. D. Reeves, and J. S. Murphy (1998), Are north-south structures an ionospheric manifestation of bursty bulk flows?, *Geophys. Res. Lett.*, *25*, 3737, doi:10.1029/98GL02692.

Heppner, J. P., and N. C. Maynard (1987), Empirical high-latitude electric-field models, *J. Geophys. Res.*, *92*, 4467, doi:10.1029/JA092iA05p04467.

Hsu, T. S., and R. L. McPherron (2003), Occurrence frequencies of IMF triggered and nontriggered substorms, *J. Geophys. Res.*, *108*(A7), 1307, doi:10.1029/2002JA009442.

Janzhura, A., O. Troshichev, and P. Stauning (2007), Unified *PC* indices: Relation to isolated magnetic substorms, *J. Geophys. Res.*, *112*, A09207, doi:10.1029/2006JA012132.
Kan, J. R., and L. C. Lee (1979), Energy coupling function and solar wind-magnetosphere dynamo, *Geophys. Res. Lett.*, *6*, 577, doi:10.1029/GL006i007p00577.
Kauristie, K., J. Weygand, T. I. Pulkkinen, J. S. Murphree, and P. T. Newell (1999), Size of the auroral oval: UV ovals and precipitation boundaries compared, *J. Geophys. Res.*, *104*, 2321, doi:10.1029/1998JA900046.
King, J. H., and N. E. Papitashvili (2005), Solar wind spatial scales in and comparisons of hourly Wind and ACE plasma and magnetic field data, *J. Geophys. Res.*, *110*, A02104, doi:10.1029/2004JA010649.
Kullen, A., and T. Karlsson (2004), On the relation between solar wind, pseudobreakups and substorms, *J. Geophys. Res.*, *109*, A12218, doi:10.1029/2004JA010488.
Kullen, A., S. Ohtani, and T. Karlsson (2009), Geosynchronous signatures of auroral substorms preceded by pseudobreakups, *J. Geophys. Res.*, *114*, A04201, doi:10.1029/2008JA013712.
Lockwood, M., M. Hairston, I. Finch, and A. Rouillard (2009), Transpolar voltage and polar cap flux during the substorm cycle and steady convection events, *J. Geophys. Res.*, *114*, A01210, doi:10.1029/2008JA013697.
Lyons, L. R., T. Nagai, G. T. Blanchard, J. C. Samson, T. Yamamoto, T. Mukai, A. Nishida, and S. Kokubun (1999), Association between Geotail plasma flows and auroral poleward boundary intensifications observed by CANOPUS photometers, *J. Geophys. Res.*, *104*, 4485, doi:10.1029/1998JA900140.
Nakamura, M., D. N. Baker, T. Yamamoto, R. D. Belian, E. A. Bering III, J. R. Benbrook, and J. R. Theall (1994), Particle and field signatures during pseudobreakup and major expansion onset, *J. Geophys. Res.*, *99*, 207, doi:10.1029/93JA02207.
Ohtani, S., et al. (1993), A multi satellite study of a pseudo-substorm onset in the near-Earth magnetotail, *J. Geophys. Res.*, *98*, 19,355, doi:10.1029/93JA01421.
Partamies, N., et al. (2003), A pseudo-breakup observation: Localized current wedge across the postmidnight auroral oval, *J. Geophys. Res.*, *108*(A1), 1020, doi:10.1029/2002JA009276.
Pulkkinen, T. I., M. Palmroth, E. I. Tanskanen, P. Janhunen, H. E. J. Koskinen, and T. V. Laitinen (2006), New interpretation of magnetospheric energy circulation, *Geophys. Res. Lett.*, *33*, L07101, doi:10.1029/2005GL025457.
Reiff, P. H., R. R. Spiro, and T. Hill (1981), Dependence of polar cap potential on interplanetary parameters, *J. Geophys. Res.*, *86*, 7639, doi:10.1029/JA086iA09p07639.
Rich, F., and M. Hairston (1994), Large-scale convection patterns observed by DMSP, *J. Geophys. Res.*, *99*, 3827–3844, doi:10.1029/93JA03296.
Rostoker, G. (1998), On the place of the pseudo-breakup in a magnetospheric substorm, *Geophys. Res. Lett.*, *25*, 217, doi:10.1029/97GL03583.
Sergeev, V. A., T. I. Pulkkinen, and R. J. Pellinen (1996), Coupled-mode scenario for the magnetospheric dynamics, *J. Geophys. Res.*, *101*, 13,047, doi:10.1029/95JA03192.
Sundberg, T., L. G. Blomberg, and J. A. Cumnock (2008), Statistical analysis of the sources of the cross-polar potential for southward IMF, based on particle precipitation characteristics, *Geophys. Res. Lett.*, *35*, L08103, doi:10.1029/2008GL033383.
Torr, M. R., et al. (1995), A far ultraviolet imager for the international solar-terrestrial physics mission, *Space Sci. Rev.*, *71*, 329, doi:10.1007/BF00751335.
Troshichev, O. A., and V. G. Andrezen (1985), The relationship between interplanetary quantities and magnetic activity in the southern polar cap, *Planet. Space Sci.*, *33*, 415, doi:10.1016/0032-0633(85)90086-8.
Troshichev, O. A., A. Janzhura, and P. Stauning (2006), Unified PCN and PCS indices: Method of calculation, physical sense, and dependence on the IMF azimuthal and northward components, *J. Geophys. Res.*, *111*, A05208, doi:10.1029/2005JA011402.

J. A. Cumnock, T. Karlsson, A. Kullen, and T. Sundberg, Space and Plasma Physics, School of Electrical Engineering, Royal Institute of Technology, Teknikringen 31, Stockholm SE-10044, Sweden. (kullen@kth.se)